Hovering Rotor FM of the URBAN-Rescue Wind Tunnel Model

Berend G. van der Wall, DLR Institute of Flight Systems, Braunschweig, Germany
Oliver Schneider, DLR Institute of Flight Systems, Braunschweig, Germany
Gunther A. Wilke, DLR Institute of Aerodynamics and Flow Technology, Braunschweig, Germany

Abstract

In 2024 the first test of a new Mach-scaled helicopter model for the medium-size low speed wind tunnel in Braunschweig was performed. This paper focuses on hovering rotor experimental data analysis and validation by comprehensive as well as computational fluid dynamics codes. Very good agreement is found between the different codes and experimental data for thrust, power and figure of merit. Stall characteristics are different in the codes and reasons are identified.

1. NOTATION

Symbols

a	Speed of sound, m/s
c	Blade chord, m
C_T, C_P	Thrust and power coefficient
C_n, C_t, C_m	Normal force, tangential force and moment coefficient
FM	Figure of merit
h, w	Height, width, m
M	Mach number
N_b	Number of blades
p	Static air pressure, hPa
P	Power, kW
r	Non-dimensional radial coordinate
r_a	Begin of airfoiled sections, root cut-out
r_{tw}	Zero twist radial coordinate
R	Rotor radius, m
t	Blade thickness, m
T	Rotor thrust, N; air temperature, °C
V	Velocity, m/s
y, z	Blade tip position in-plane and out-of-plane relative to precone, m
$\alpha, \alpha_0, \alpha_{ss}$	Section, zero lift and stall angle of attack, deg
β_p	Precone angle, deg
λ_i, λ_{i0}	Induced inflow ratio, mean value of it
ν	Frequency ratio
ρ	Air density, kg/m³
Θ	Pitch angle, deg
ω_n	Natural frequency, rad/s
Ω	Rotor rotational frequency, rad/s

Subscripts

75	At $r = 0.75$
a	Aerodynamic
el	Elastic deformation
hub	Related to rotor hub
max	Maximum
ref	Reference condition
tip	Blade tip
tw	Blade twist
WT	Wind tunnel

Acronyms

CFD	Computational Fluid Dynamics
DAQ	Data acquisition system
DLR	German Aerospace Center
DNW	German-Dutch Wind Tunnels
FLOWer	DLR's block structured Navier–Stokes solver
NWB	Low-Speed Wind Tunnel Braunschweig
RPM	Revolutions per minute
S4	DLR's comprehensive rotor code
TEDAS	Throughput Enhanced Data Acquisition System

2. INTRODUCTION

In June 2024 the first test of a new helicopter model for the medium-size low speed wind tunnel in Braunschweig was performed. This test was a milestone within DLR's project URBAN-Rescue, lasting from 2020-2024, which is part of DLR's guiding concept 4 "The Rescue Helicopter 2030", aiming at the design of a fast rescue helicopter. A slim aerodynamically shaped fuselage was designed during a predecessor project and tested in 2020 without a rotor for comparison with a reference fuselage typical for today's rescue helicopters.

The 2024 test included a newly built Mach-scaled main rotor and stub wings on the fuselage. Different configurations were performed: isolated fuselage with or without stub wings, and both setups with the rotor. Operational conditions ranged from hover to high speed and the experiments included measurements of rotor, fuselage and wing balances, blade pitch angles, pitch link loads, blade bending moments, blade pressure data, and acoustic radiation via microphone arrays.

This paper focuses on hovering rotor experimental data analysis for different configurations and validation by comprehensive as well as computational fluid dynamics (CFD) codes. Hovering measurements are of permanent interest as reflected by the AIAA Rotorcraft Hover Prediction Workshop initiated at an AIAA SciTech special hover session held in 2014, which now includes four different rotors in hovering condition.

The rotor tested within URBAN-Rescue is a Mach-scaled hingeless rotor with radius of 0.812 m. The blade planform and twist are derived from the articulated ONERA 7AD 2.1 m radius rotor blade that had been used in many wind tunnel tests, e.g. Ref. 1, using the same airfoils. A dynamical scaling, however, could not be achieved, hence it represents a stiff in-plane rotor blade.

This is one of the first publications using the URBAN-Rescue wind tunnel test data for code validations. Preliminary wind tunnel test data were presented in Ref. 2. Hover studies with S4 applied to the HART II rotor have been published in Ref. 3. Hover computations using CFD were published in Refs. 4,5,6.

3. HARDWARE, TEST AND SOFTWARE

3.1. Helicopter model

The new helicopter model was designed to perform tests in the DNW-NWB wind tunnel with a cross-section of 3.25 m x 2.8 m. The model is hydraulically driven where the motor torque is transmitted by a tooth belt drive to the rotor shaft. To separate the measurement of different load sources, it was necessary to use different balances (see Figure 1). The 6-component rotor balance (RUAG 192-6D) is directly attached to the belly sting and carries the complete base structure including hydraulic motor and drive system as well as the rotor system.

For measuring the fuselage loads an integrated cylindrical 6-component balance of type Task 1.25" is mounted behind the rotor shaft. To guarantee independent measurements of rotor and fuselage loads the connection of the fuselage balance to the sting attachment point is done via two structure side plates outside of the basic structure. To optionally install wing stubs one 5-component wing balance can be mounted to each of the side plates and measure independently from rotor and fuselage balance.

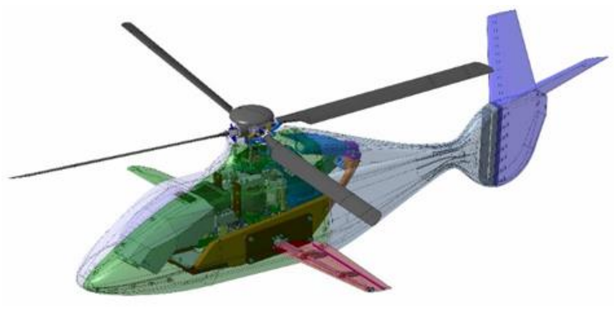

Figure 1: Basic setup of the wind tunnel model.

The fuselage shells as well as the wings were manufactured using 3D-printing techniques with additional reinforcements (see Figure 2). Background information about the model design, model scaling, and manufacturing of parts and pre-testing are given in Ref. 7.

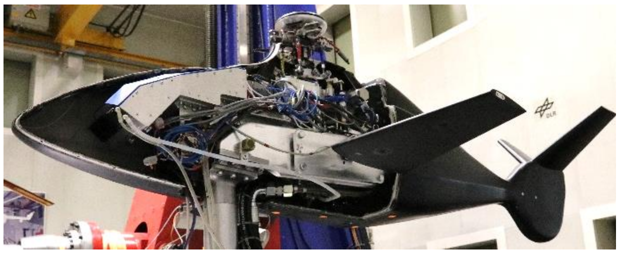

Figure 2: Wind tunnel model inner structure.

In the rotating frame a new in-house developed rotational data acquisition system is used to acquire the pitch link force, the pitch angle, torsion moment as well as the bending moments in flap and lag direction for each rotor blade. Furthermore, two rotor blades were equipped with dynamic pressure sensors, one with 8 sensors on the upper side along span at 10 % chord, one with 14 sensors in a cross section at 70 % radius. Details of the rotor and blade characteristics are given in Table 1. More information about the manufacturing of the rotor blades can be found in Ref. 8.

Table 1: Rotor and blade characteristics.

Characteristic	Symbol	Value
Number of blades	N_b	4
Radius	R	812 mm
Mean chord	c	57 mm
Solidity	σ	0.08938
Blade tip chord	c_{tip}/c	0.3333
Root cutout	r_a	0.2346
Zero twist radius	r_{tw}	0.7500
End of inner airfoil	r_1	0.7537
Begin outer airfoil	r_2	0.9015
Begin parabolic tip	r_3	0.9474
Inner airfoil	OA	213
Outer airfoil	OA	209
Twist offset, outer airfoil	$\Delta\Theta_{tw}$	2.95 deg
Blade twist	Θ_{tw}	-8.387 deg
Precone angle	β_p	2.0 deg
Ref. rot. frequency	Ω_{ref}	259.8 rad/s
Test rot. frequency	Ω	$0.75\Omega_{ref}$
1st flap frequency	$\nu_{F1} = \omega_{F1}/\Omega$	1.258
1st lag frequency	$\nu_{L1} = \omega_{L1}/\Omega$	1.729
1st torsion frequency	$\nu_{T1} = \omega_{T1}/\Omega$	6.424

The blade planform, thickness, twist and airfoil distribution are shown in Figure 3. Twist is given using the chord line definition of the respective ONERA/Aerospatiale airfoils OA213 and OA209 with 13% and 9% thickness.

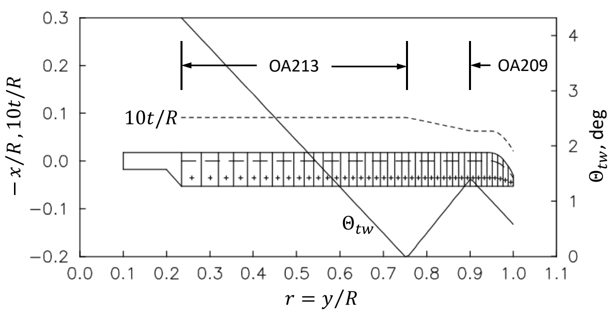

Figure 3: Planform, thickness, twist and airfoil distribution of the model rotor blade.

The fan diagram of the hingeless rotor blade is shown in Figure 4 for rotational frequencies up to 100 % RPM Ω_{ref}. At 75 % RPM all modes are well separated from each other.

Data from sensors in the non-rotating frame were acquired by an in-house developed data acquisition system TEDAS III. This DAQ is specially designed for rotor-triggered measurements. Key specifications of the TEDAS III system are:

- 496 channels analogue DAQ
- Simultaneous sampling
- 1024/2048 samples per revolution
- 16-bit ADCs
- Rotor triggered measurement or fixed frequency

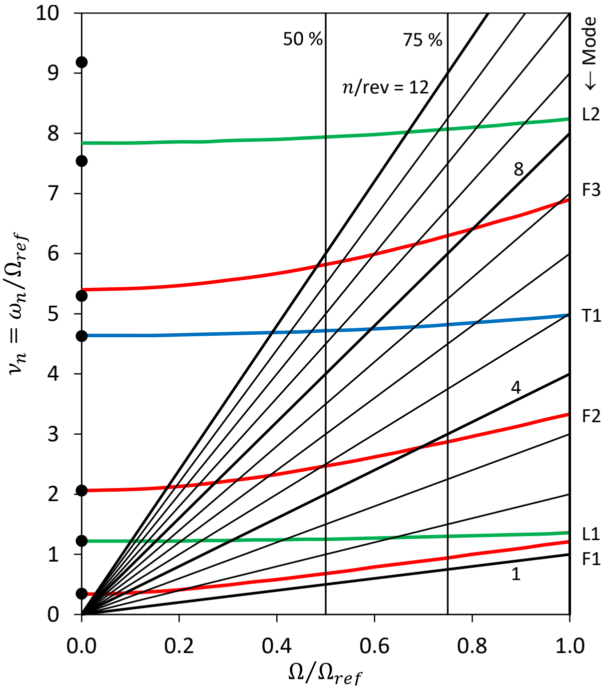

Figure 4: Fan diagram of the model rotor up to nominal speed $\Omega_{ref} = 259.8$ rad/s = 100 % RPM. Red: flap modes, green: lag modes, blue: torsion modes.

To measure the sensors in the rotating frame a newly developed wireless rotational DAQ system was used for the first time, Ref. 9. The rotational DAQ is placed on top of the main rotor head in an ellipsoid shaped housing carrying the electronic components. A small slip ring with a limited number of channels is used for transfer of electrical power to the rotating parts as well as the 1P signal from the non-rotating azimuth encoder. In total 48 channels can be measured with a fixed data rate of up to 50 kHz, which leads to an azimuthal resolution of at least 1024/rev. The synchronization between the rotating and non-rotating data (captured sequentially) is based on the rotor azimuth position determined from the 1P signal.

3.2. Wind Tunnel Test

The DNW low-speed atmospheric wind tunnel in Braunschweig (NWB) was used in an open-jet configuration. Its properties are given in Table 2 and due to the large hub height above ground it can be assumed as operating out-of-ground conditions, Figure 5. However, despite the size of the surrounding test hall, due to its closed walls some unknown recirculation will develop in hovering condition. This recirculation will be in proportion to the square root of the rotor thrust, following momentum theory. Therefore, with increasing thrust the operational condition will effectively be a climb condition with a velocity increasing in proportion to the rotor's induced velocity, i.e. also proportional to the square root of the rotor's thrust.

Table 2: DNW-NWB characteristics.

Characteristic	Symbol	Value
Maximum wind speed	V_{max}	80 m/s
Nozzle width	w_{WT}	3.25 m
Nozzle height	h_{WT}	2.8 m
Hub height above ground	h_{hub}	3.4 m
Ground separation ratio	h_{hub}/R	4.19

Figure 5: Model in hover condition in DNW-NWB.

To get acoustic data from below the model two microphone arrays were installed with 28 microphones each, one on the advancing side of the rotor on the upstream location and one on the retreating side on the downstream location as shown in Figure 5.

Although the blades are safe with respect to the expected loads of the entire operational envelope, blade attachment components of the hingeless rotor system were found not fulfilling the requested safety factors. Therefore, the operational frequency of rotation for the first NWB test with spinning rotor was reduced to 75 % of the reference value. In order to obtain the same range of advance ratios, the maximum wind tunnel speed was accordingly reduced to now $V_{\infty,max} = 60$ m/s.

3.3. S4 Comprehensive code

The DLR comprehensive analysis tool, S4, is a high resolution, 4th generation comprehensive rotor simulation code, Refs. 6,11. The finite-element-based structural dynamics modeling in S4 is based on Houbolt and Brooks equations, Ref. 12. The beam element has ten degrees of freedom. A semiempirical formulation of the airfoil coefficients based on the Leiss method, Ref. 13, is used for unsteady blade motion, but further modification is made for the BVI problem. The fuselage interference flow effect is included at the blade sections using a semi-empirically derived formulation from the potential theory, Ref. 14.

The Mangler/Squire global wake model, Ref. 15, is used here for performance and vibration estimates, but an extended version of the Beddoes' prescribed wake geometry formulation, Ref. 16, with multiple trailers could be used especially for noise predictions, accounting for wake deflections due to harmonic rotor loading. Special treatment of blade tip losses is performed in the range $r > 0.9$ and at the blade root via additional induced inflow simulating a tip vortex and leading to zero-lift angle of attack at the tip (and root), Ref. 3. Trim is performed with an azimuth increment of 1 deg, and the simulation uses the first six modes for a modal analysis.

3.4. FLOWer CFD code

The DLR-CFD approach is utilizes on the coupling of the DLR legacy flow solver FLOWer, Ref. 17. For simplicity, the blade has been assumed rigid, however, torsion deformation at the tip was not measured. The inviscid fluxes are resolved using a 4th-order upwind scheme (SLAU2 with FCMT), Ref. 18. The turbulence model SA-DDES-R, Refs. 19,20, is applied for the computation of the eddy viscosity and transition is empirically predicted, Ref. 21. A dual time-stepping approach with a timestep equivalent to 0.5 deg of a revolution is used.

Periodicity is exploited and only one blade is modelled with the neglection of everything else, e.g. fuselage, support, wind tunnel walls. An inviscid Euler wall is placed in the rotational center to suppress the initial upwash there. The total grid features 3 million grid points and is built in a similar fashion as in Refs. 4,5,6. The blade surface consists of 128 cells in chordwise and spanwise direction, the boundary layer is roughly resolved with 30 cells with the overall grid setup having 2.6 million cells. The far field extends to 6 radii at the top and bottom of the rotor with the Spalart viscous jet function applied as the boundary condition, Ref. 22. Each case was run for 50 revolutions, which led to steady results up to 14 degrees collective after roughly 25 revolutions. Beyond this collective angle, seemingly chaotic behavior was observed, but the averaged thrust leveled out. The peak-to-peak thrust variation remains roughly 13 % of the corresponding mean thrust of the last revolution for the 22 deg collective case. The far-field boundary condition does not include the closed walls all around the test chamber, which cause a mild recirculation. Such effects could be accounted for, Ref. 23, but at tremendous computational cost and were not included here.

4. RESULTS

4.1. Hover test data and corrections

During the model preparation phase, it was detected that the rotor balance data are influenced by the hydraulic lines due to deformations of the hoses, which leads to erroneous results. Data from a rotor spin-up with blade stubs instead of rotor blades can be used for a correction of this influence. Most impact could be found for the vertical force F_z and the rotor moments, while the side force and longitudinal force are not affected. Depending on the hydraulic pressure p_V an increasing error can be observed, for F_z with an asymptotic trend as approximation (App.), as shown in Figure 6.

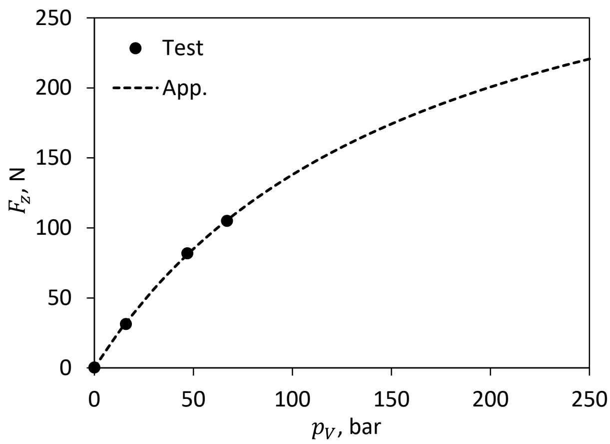

Figure 6: Vertical rotor force.

Using an asymptotic correction function for the vertical force and the in-plane moments and a linear correction function for the torque component the errors in the rotor balance data can be corrected depending on the hydraulic pressure, which is measured by a sensor near the motor location.

Test data for the hover results were acquired by a variation of collective blade pitch from $\Theta_{75} = 0.4$ deg to $\Theta_{75} = 16$ deg in increments of about 2 deg. The rotor thrust variation was between 45 N and 885 N. For the final results the pressure correction was applied to the data as well as a correction of a slight drift in the rotor balance data using an approach with linear deviation over time and two reference measurements, one before the thrust variation and one afterwards.

4.2. Simulation results

The S4 comprehensive code was used with elastic blade modeling including 3 flap, 2 lag and 1 torsion mode while FLOWer was applied with rigid blades. Trim was also performed differently. Because of faster computation results, FLOWer was used with prescribed collective control angles from $\Theta_{75} = 0$ deg to 22 deg in increments of 2 deg. In contrast, S4 was trimmed to thrust from $T = 100$ N to 900 N (near maximum thrust) in increments of 100 N. For larger control angles a trim to power was performed in increments of 5 kW. Atmospheric data used in the simulations were chosen by the authors prior to test data availability and are given in Table 3, the differences are considered negligible.

Table 3: Atmospheric conditions used in simulations.

Characteristic		Test	S4	FLOWer
Air temperature, °C	T	19.7	20.0	22.3
Air pressure, hPa	p	1001	1015	999.4
Air density, kg/m³	ρ	1.186	1.206	1.178
Sonic speed, m/s	a	343.0	343.9	344.8
Tip Mach number	M_{tip}	0.4611	0.4602	0.4587

Results for thrust and power development are shown in Figure 7. For S4, the onset of rotor stall is observed at around $\Theta_{75} \approx 20$ deg, whereas for FLOWer stall onset is observed already at roughly $\Theta_{75} \approx 15$ deg in Figure 7a. However, where S4 clearly shows the rotor stall, FLOWer shows still an increase in thrust. In general, the agreement is very good in the linear aerodynamic regime, despite the significant differences in modeling, which will be discussed in more detail later. The Mangler/Squire downwash model is used in S4, which generates low inflow values inboard and the highest downwash occurs around 80 % radius. Therefore, this model is usually leading to inboard stall first, which is felt as “mild stall” for the entire rotor due to the low dynamic pressure there. Opposing this, in the FLOWer simulation, the tip-vortex of the previous vortex triggers the separation at the outboard of the rotor while the inboard stations still continue to carry.

The power of test and simulations is shown in Figure 7b. In attached flow, both S4 and FLOWer are very close to the test data, while from stall onset on FLOWer results in higher power than S4 and agrees better with test data.

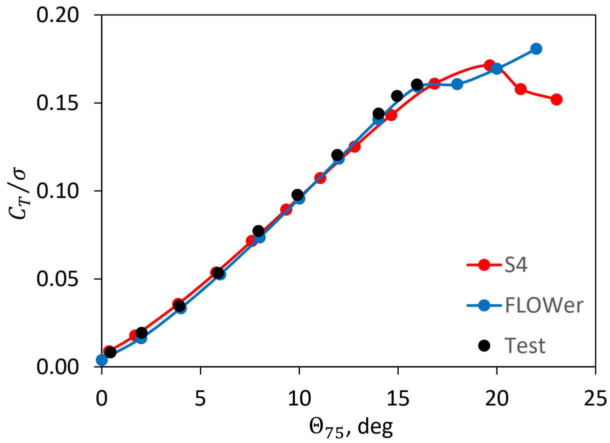

(a) Rotor thrust

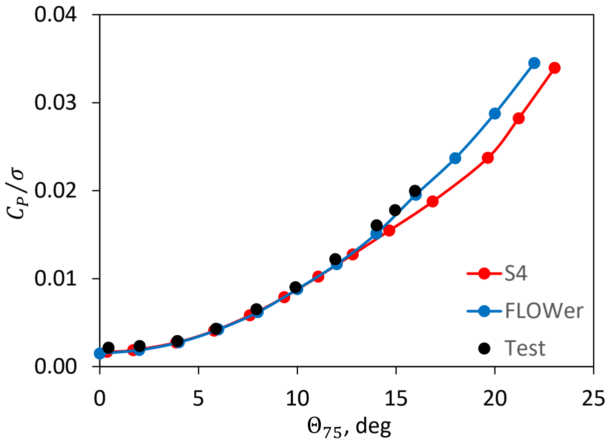

(b) Rotor power

Figure 7: Rotor thrust and power versus collective control angle.

The resulting figure of merit is given in Figure 8. The agreement between the two codes is very good except for two regions: first, around moderately low thrust around $C_T/\sigma = 0.05$ in the attached regime, where the thrust predicted by S4 is slightly larger than that of FLOWer. Second, near maximum thrust and larger blade loadings $C_T/\sigma = 0.14$ where FLOWer predicts a further increase in thrust while S4 shows a loss of thrust as already seen in in Figure 7a.

Some of the differences may be attributed to the use of the Mangler downwash model, some may be caused by blade flexibility in S4, while FLOWer used rigid blades. S4 results of blade tip deflections are shown in Figure 9. The blade tip displacements in flap and torsion computed by S4 are shown versus rotor thrust in Figure 9a. As expected, the flap displacement is essentially linear with the rotor thrust, while torsion, is very moderate in attached flow, but progressively becoming negative once stall develops.

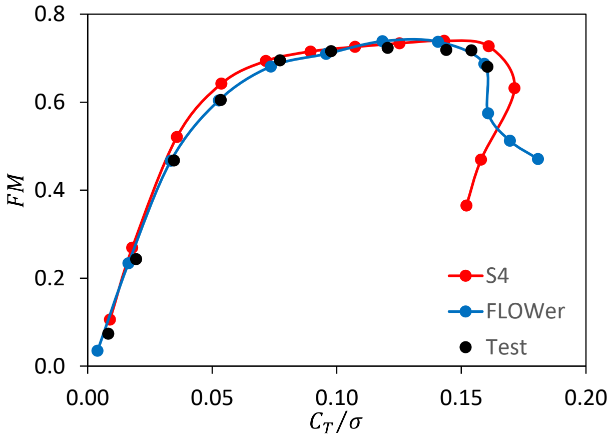

Figure 8: Rotor figure of merit.

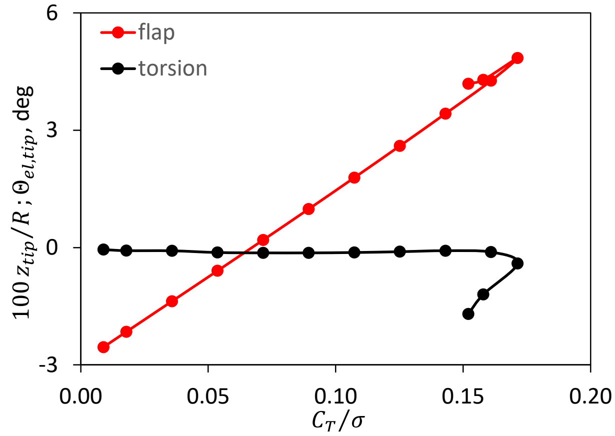

(a) flap and torsion

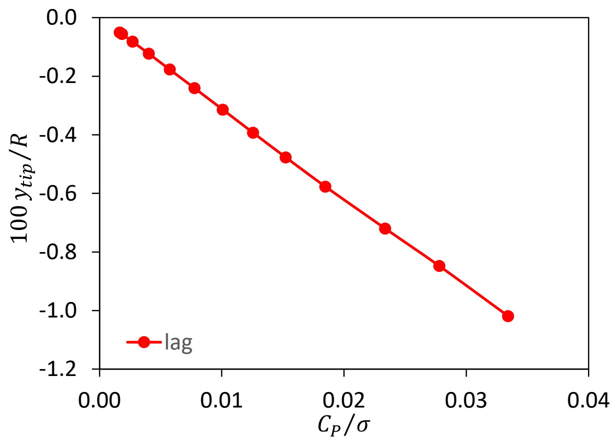

(b) lag

Figure 9: Elastic blade tip deflections, S4 results.

Because rotor stall in S4 is associated with a loss of thrust and a radial re-distribution of blade lift is expected depending on where stall develops, the flap displacement in the stalled regime becomes slightly off the linear line. The elastic lag displacement is shown versus power instead of thrust in Figure 9b, because it is expected to vary linearly with power. This holds even for the stalled regime (last two points).

Finally, radial distributions of non-dimensional section normal force (pos. up), tangential force (pos. forward) and pitching moment (pos. nose up) averaged over the last revolution are shown in Figure 10 for three different thrust levels, indicated by the collective control angles: $\Theta_{75} = 6$ deg represents a thrust of ca. 300 N, 14 deg is equivalent to ca. 800 N and 20 deg to ca. 950 N. The latter is about the maximum thrust in S4 results and already in the rotor stall regime for FLOWer. The aerodynamic coefficients are represented in the form multiplied by $M^2\, c/c_{ref}$ in order to be able to directly compare the sectional forces and moments. The Mach number is based on the sectional circumferential velocity for both codes for reasons of better comparability.

In Figure 10a, the normal force distribution is shown. It must be recognized that FLOWer includes orthogonal blade-vortex interaction with the tip vortex of the preceding blade, located near $r = 0.9$. It induced upwash on the right of it and downwash on the left, leaving a wave in the radial distribution which is not present in S4 results, because the Mangler downwash model does not include such discrete vortices. Due to its low induced velocities inboard, the Mangler model leads to greater angles of attack inboard and hence larger section lift than the FLOWer results. For the highest thrust, S4 is not yet developing stall near the blade tip, while FLOWer shows a significant loss of normal force there, indicating blade tip stall. For attached flow, both codes show fairly good agreement.

The chord force distribution is given in Figure 10b. Despite larger differences between the two codes' results the trends are similar to those observed in the normal force distributions. This is not the case for the region near the tip itself, where strong three-dimensionality of the flow is present due to the free end of the blade and further exaggerated by the large sweep of the blade tip. The essentially two-dimensional approach of S4 – despite an advanced continuous tip loss model – cannot account for full three-dimensional flows and larger differences to FLOWer were expected and actually are present.

This is also true for the section moment distribution shown in Figure 10c. The moment is very sensitive to stall and due to the pressure point moving aft of the quarter chord point in stalled condition quickly develops much larger nose-down moments than in attached flow. The formerly made hypothesis that S4 due to the inflow model might stall first in inboard regions is confirmed here, and also the stall of FLOWer first near the blade tip.

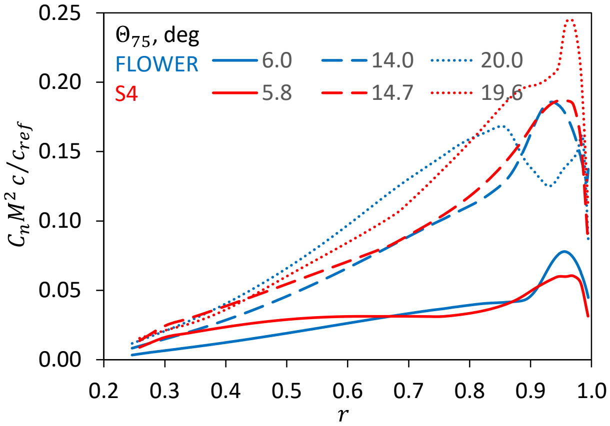

(a) normal force (pos. up)

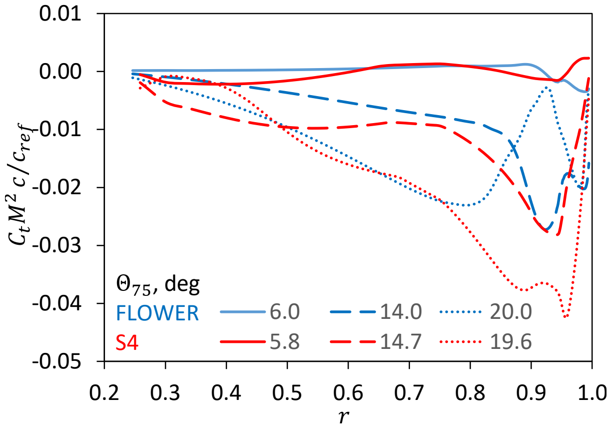

(b) tangential force (pos. forward)

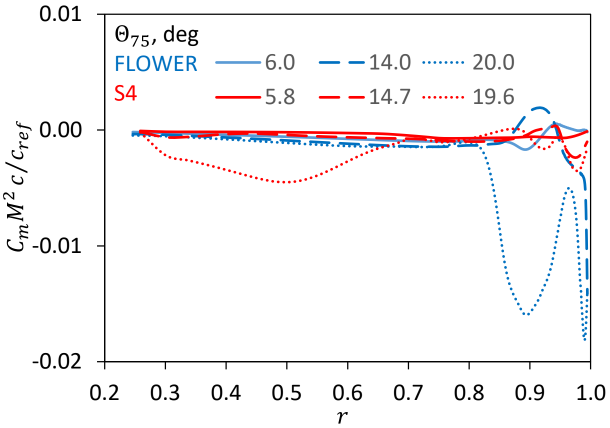

(c) moment (pos. nose-up)

Figure 10: Radial distribution of aerodynamic loads.

Further information can be obtained from a comparison of induced inflow ratio distributions of these cases, shown in Figure 11 (pos. downwards). The S4 results include root and tip losses by means of virtual root and tip vortices that progressively rise towards the tip to generate the zero-lift angle of attack at the tip. The Mangler-Squire downwash model does not include these tip losses and its distribution is sketched by the black lines. A tip vortex from the preceding blade is not represented by the Mangler model.

In case of FLOWER results data were extracted between successive blades. Therefore, they do not include the tip and root vortex induced inflow on itself, but they show the preceding blade's tip vortex with a center located at $r \approx 0.95$, which will move further inboard until interacting with the following blade. Note that the thrust of the three cases slightly differs between S4 and FLOWER, see Figure 7a. Also for the largest collective control angle in Figure 11 stall developed in FLOWER results in the region $r > 0.8$, see Figure 10a and c, which leads to strong turbulence in the air and the induced inflow distribution there is only an instantaneous figure, while the downwash of the Mangler model in S4 remains steady even in case of airfoil stall.

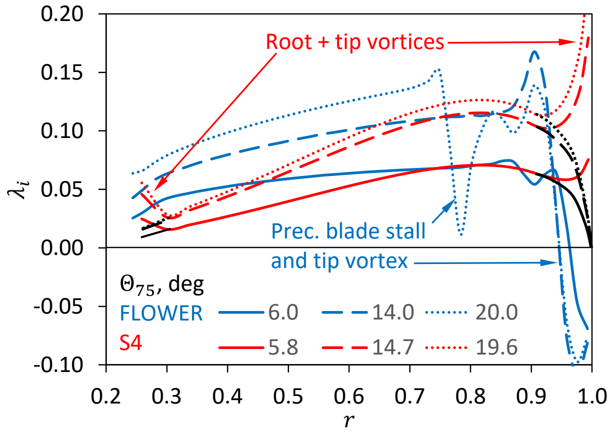

Figure 11: Radial distribution of induced inflow ratios.

In the region $0.7 < r < 0.9$ the Mangler model and FLOWER agree pretty well, more inboard the FLOWER inflow is generally larger than that of the Mangler model and near the blade tip for $r > 0.9$ no direct comparison can be made. Removing the tip vortex individual contribution in the FLOWER results suggests some similarity with the pure Mangler model sketched in black lines. The mean induced inflow ratio from momentum theory is not plotted for comparison with S4 and FLOWER, but given in Table 4. The Mangler model in S4 (without the tip loss contributions) has a mean value of λ_{i0} as in Table 4, and the FLOWER data that may be estimated from the respective curves in Figure 11 appear close to these.

Table 4: Mean induced inflow ratio λ_{i0} by momentum theory, S4.

Θ_{75}, deg	5.8	14.7	19.6
C_T/σ	0.0537	0.143	0.171
λ_{i0}	0.049	0.079	0.087

For S4, the radial distribution of the aerodynamic angle of attack at the blade sections provides the final proof of regions within attached flow or exceeding stall, because the Leiss airfoil model includes the steady stall angle of attack. These data are given in Figure 12. In agreement with Figure 10c stall is present inboard of $r = 0.7$ and a bit around $r = 0.9$. Due to the tip loss model the very tip itself will never stall in S4, because the angle of attack approaches zero lift angle fo attack there: $\alpha_a \rightarrow \alpha_0$. In addition, the parabolic tip introduces a very large leading edge sweep angle up to 60 deg, aerodynamically a large sweep angle, which causes a large stall delay, shifting the stall angle of attack to over 25 deg (black line for $r > 0.9$).

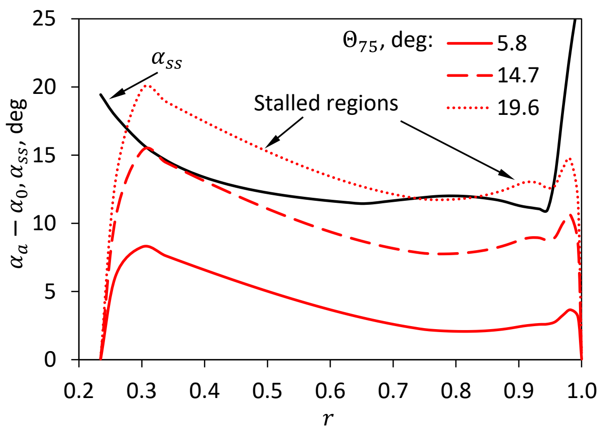

Figure 12: Radial distribution of section angle of attack and section stall angle of attack, S4 results.

Because the angle of attack is strongly depending on the induced inflow ratio distribution, the selection of inflow model affects the location of stall onset being inboard or outboard. The Mangler model with rather small inboard inflow often leads to inboard stall onset, while constant inflow from momentum theory, but also prescribed or free-wake methods mostly generate stall onset outboard, see Ref. 3.

To further support the hypothesis or stalled regions in FLOWer results, the vorticity fields of the CFD results are plotted in Figure 13 by means of the Q-criterion. For the lowest collective control angle shown in Figure 13a, a very steady flow field is observed with some of the wake still visualized by the Q-criterion. A root vortex is also found, which is shifted more outboard due to the presence of the Euler wall.

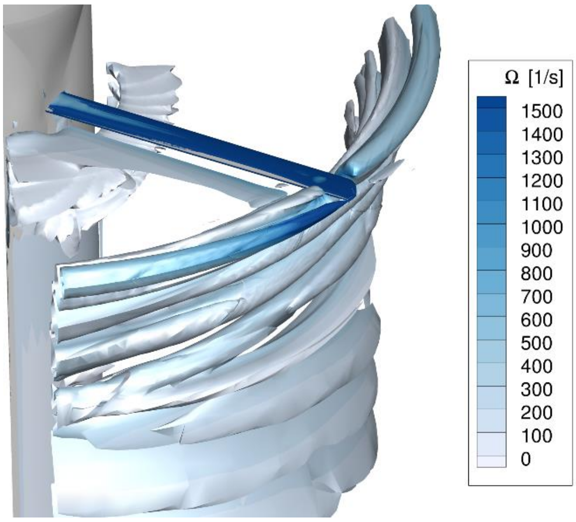

(a) $\Theta_{75} = 6°$

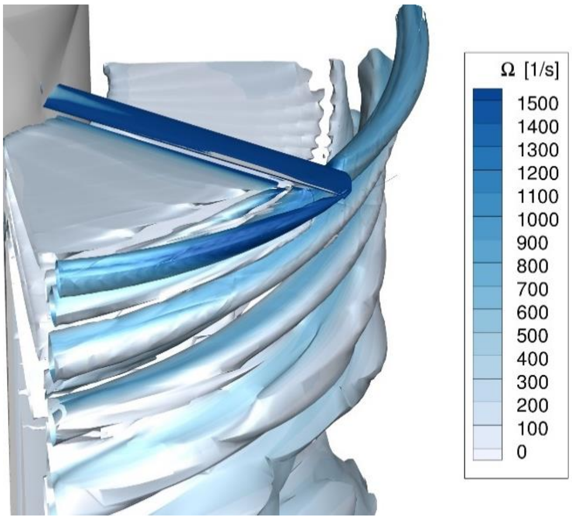

(b) $\Theta_{75} = 14°$

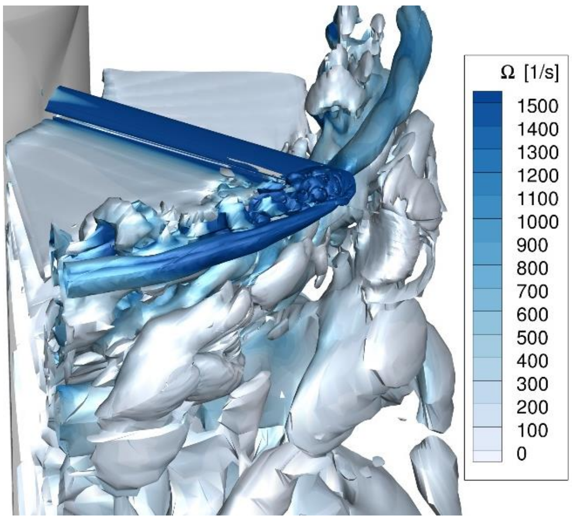

(c) $\Theta_{75} = 20°$

Figure 13: Vorticity plots of CFD results at different collective angles. All plotted at same Q-criterion.

The middle collective control angle setting, Figure 13b, shows a stronger wake sheet and tip vortex, but also a greater interaction between the tip-vortices below the rotor.

For the highest collective control angle given in Figure 13c, the stall vortex at the tip can also be found which mixes with the primary tip vortex of the blade, but is also fed by the incoming tip vortex of the previous blade. This leads to a greater interaction between the individual tip vorticites and the dissolution into secondary vortex structures. These are likely underresolved on this relatively coarse grid, but nevertheless, it is believed that the mechanism is already captured on a reasonable level due to the application of a low-dissipation higher order scheme, the skipping of overset interpolation and the DDES-R extensions applied to the SA turbulence model.

5. CONCLUSIONS

1. First wind tunnel hover tests of DLR's modular helicopter model have been presented alongside numerical investigations with DLR's S4 comprehensive code and CFD simulations with DLR's legacy FLOWer code.

2. The wind tunnel rotor balance data required substantial corrections due to systematic errors, because of the construction with hydraulic hoses bypassing the balance. The rotor hydraulic pressure causes non-linear drift of all forces and moments. Additionally, the balance undergoes drifts in all forces and moments during time of operation.

3. The results of the wind tunnel data could be reproduced to a reasonable degree by both codes. Both simulations overpredicted the maximum Figure of Merit of the experiment, which is believed to be associated to a (mild) recirculation occurring in the closed-wall test hall. Similar observations have been made previously with a larger rotor in the DNW large low-speed facility and in DLR's rotor preparation hall. CFD is capable of prediction recirculation effects, but to an enormous computing cost and therefore was not used in this study.

4. At higher thrusts, the CFD results showed better agreement with the experiment than the comprehensive code results. It was identified that the main cause for this is that the Mangler-Squire inflow model in the comprehensive code does not

account for the incoming tip vortex of the previous blades. This, in combination with the general highly unsteady nature of stall, leads to the better predictability of the results by CFD. Prescribed or free-wake methods for the induced flow field should improve the comprehensive code results in this aspect.

5. Despite the good results, it is believed that on the CFD side, results and correlation with the experiment can be further improved through the application of elasticity, modelling of the complete test setup (fuselage, sting, wind tunnel), and inclusion of more grid points and finer time steps. However, the improvements will likely not be worth the effort. It seems that the lack of elasticity (nose-down torsion will increase hover efficiency) may be compensated for by the recirculation due to closed wind tunnel walls (leading to a decrease of hover efficiency).

Future work on the simulation's side will focus on improving comprehensive code results through modelling the tip vortex, whereas CFD results will aim to include elasticity, and potentially both codes with inclusion of the fuselage. On the experimental side, full RPM results are planned to reach the proper Mach scale. Such experiments have been made during the NWB test preparation in DLR's rotor test hall, also at half RPM.

Author contact:

Berend van der Wall berend.vanderwall@dlr.de
Oliver Schneider oliver.schneider@dlr.de
Gunther Wilke gunther.wilke@dlr.de

6. REFERENCES

1. van der Wall, B.G., Kessler, C., Delrieux, Y., Beaumier, P., Gervais, M., Hirsch, J.-F., Pengel, K., Crozier, P., "From Aeroacoustics Basic Research to a Modern Low Noise Rotor Blade," *Journal of the American Helicopter Society*, Vol. 62, (4), 2017, pp. 042001-1-16. DOI: 10.4050/JAHS.62.042001.

2. Brehl, E., and Schneider, O., "Evaluation of wind tunnel test data from a helicopter model with novel fuselage geometry and additional passive lift devices," 23rd DGLR STAB-Symposium, Nov. 13-14, Regensburg, Germany, 2024.

3. van der Wall, B.G., "Influence of rotor inflow, tip loss and aerodynamics modeling on the maximum thrust computation in hover," *MDPI Aerospace*, Special Issue: Vertical Lift: Rotary- and Flapping-Wing Flight, Vol. 11, (357), 2024, pp. 1-23. DOI: 10.3390/aerospace11050357

4. Wilke, G., "Quieter and Greener Rotorcraft: Concurrent Aerodynamic and Acoustic Optimization," *CEAS Aeronautical Journal*, Vol. 12, (3), 2021, pp. 495–508. DOI: 10.1007/s13272-021-00513-x

5. Wilke, G., Bailly, J., Kimura, K., and Tanabe, Y., "JAXA-ONERA-DLR Cooperation: Results from Rotor Optimization in Hover," *CEAS Aeronautical Journal*, Vol. 13, (2), 2022, pp. 313–333. DOI: 10.1007/s13272-022-00580-8

6. Gerlach, R., "Untersuchung der aerodynamischen Eigenschaften des HART-II Hubschrauberrotors im Schwebeflug mittels CFD-Simulationen," Bachelor Thesis, Ostfalia, Hochschule für angewandte Wissenschaften, Wolfenbüttel, Germany, 2024.

7. Schneider, O., Mainz, H., Brehl, E., Henseleit-Wieser, S., and van der Wall, B.G.: "Development of a New Medium Size Helicopter Wind Tunnel Model," 50th European Rotorcraft Forum, Marseille, France, Sept. 10-12, 2024.

8. Mainz, H., Schneider, O., Bartels, R., and van de Kamp, B. "Design, Manufacturing and Testing of Highly Instrumented Rotor Blades for a Medium Size Helicopter Wind Tunnel Model," 50th European Rotorcraft Forum, Marseille, Sept. 10-12, 2024.

9. Brehl, E. and Schneider, O. "Rotational Data Acquisition for Rotorcraft Wind Tunnel Models", European Test and Telemetry Conference, Paper 3596, Toulouse, France, June 13-14, 2023.

10. van der Wall, B.G., "Analytic Formulation of Unsteady Profile Aerodynamics and its Application to Simulation of Rotors," ESA–TT–1244, 1992 (Translation of DLR–FB 90–28, 1990).

11. van der Wall, B.G., Lim, J.W., Smith, M.J., Jung, S.N., Bailly, J., Baeder, J.D., and Boyd, D.D., "The HART II International Workshop: An Assessment of the State–of–the–Art in Comprehensive Code Prediction," *CEAS Aeronautical Journal*, Vol. 4, (3), 2013, pp. 223–252. DOI: 10.1007/s13272-013-0077-9.

12. Houbolt, J.C., and Brooks, G.W., "Differential Equations of Motion for Combined Flapwise

Bending, Chordwise Bending, and Torsion of Twisted Nonuniform Rotor Blades," NACA TN 3905, 1957.

13. Leiss, U., "A Consistent Mathematical Model to Simulate Steady and Unsteady Rotor–Blade Aerodynamics," 10th European Rotorcraft Forum Proceedings, The Hague, Netherlands, Aug. 28–31, 1984.

14. van der Wall, B.G., Yin, J., "Semi-Empirical Modeling of Fuselage-Rotor Interference for Comprehensive Codes: Influence of Angle of Attack," *CEAS Aeronautical Journal*, Vol. 6, (4), 2015, pp. 557-574. DOI: 10.1007/s13272-015-0163-2.

15. Mangler, K.W., and Squire, H.B., "The Induced Velocity Field of a Rotor," ARC R&M 2642, 1950.

16. Beddoes, T.S., "A Wake Model for High Resolution Airloads," AHS/ARO 1st International Conference on Rotorcraft Basic Research, Research Triangle Park, North Carolina, Feb. 19–21, 1985.

17. Raddatz, J., and Fassbender, J.K., "Block Structured Navier–Stokes Solver FLOWer," in: Kroll and Fassbender (Eds): *Notes on Numerical Fluid Mechanics and Multidisciplinary Design: MEGAFLOW – Numerical Flow Simulation for Aircraft Design*, Vol. 89, 2005, pp. 27–44, Springer: Berlin–Heidelberg, Germany. DOI: 10.1007/3-540-32382-1_2.

18. Wilke, G., "Comparisons of Different Spatial Schemes and Limiters for Helicopter Flows," in: Dillmann et al. (Eds): *Notes on Numerical Fluid Mechanics and Multidisciplinary Design: New Results in Numerical and Experimental Fluid Mechanics XIII: Contributions of the 22nd STAB/DGLR Symposium*, Vol. 151, 2021, pp. 418–427, Springer: Berlin–Heidelberg, Germany. DOI: 10.1007/978-3-030-79561-0_40.

19. Shur, M.L., Spalart, P.R., Strelets, M.K., and Travin, A.K., "A Hybrid RANS–LES Approach with Delayed–ES and Wall–Modelled LES Capabilities," *International Journal of Heat and Fluid Flow*, Vol. 29, (6), 2008, pp. 1638–1649. DOI: 10.1016/j.ijheatfluidflow.2008.07.001.

20. Dacles–Mariani, J., Kwak, D., and Zilliac, G., "On Numerical Errors and Turbulence Modeling in Tip Vortex Flow Prediction," *International Journal for Numerical Methods in Fluids*, Vol. 30, (1), 1999, pp. 65–82. DOI: 10.1016/j.ijheatfluidflow.2008.09.004.

21. Heister, C.C., "A Method for Approximate Prediction of Laminar–Turbulent Transition on Helicopter Rotors," *Journal of the AHS*, Vol. 63, (3), 2018, pp. 1–14. DOI: 10.4050/JAHS.63.032008.

22. Jia, F., Wang, Q., and Spalart, P., "Improved Initial and Boundary Conditions for Hovering Rotor CFD Simulations," Vertical Flight Society 78th Annual Forum & Technology Display Proceedings, Fort Worth, Texas, May 10-12, 2022. DOI: 10.4050/F-0078-2022-17474.

23. Wilke, G. A., Sugawara, H., Tanabe, Y., Schneider, O. and van der Wall, Berend G., "Investigations of a boxed rotor: The STAR II rotor in DLR's test hall," 49th European Rotorcraft Forum Proceedings, Bückeburg, Germany, Sept. 5-7, 2023.